Simultaneous identification of the heat capacity and the anisotropic thermal conductivities of a Li-ion pouch cell by a non-destructive analytical approach

Sylvain Cailliez, David Chalet, Philippe Mannessiez

Simultaneous identification of the heat capacity and the anisotropic thermal conductivities of a Li-ion pouch cell by a non-destructive analytical approach

Sylvain CAILLIEZ[a]*, David CHALET[a], Philippe MANNESSIEZ[b]

[a]Ecole Centrale de Nantes, LHEEA Lab. (ECN/CNRS), 1 rue de la Noë, 44321 Nantes Cedex 3, France

[b]CRITT M2A, Rue Christophe Colomb, 62700 Bruay-la-buissière, France

*Corresponding author (sylvain.cailliez@ec-nantes.fr)

Abstract

The specifications and aging of Li-ion batteries highly depends on temperature. Battery thermal models are therefore useful to improve the thermal management of battery packs. This study presents a method to determine the heat capacity and the anisotropic thermal conductivities of a Li-ion pouch cell. A single experimental setup is devised and involves local heating of the battery with a resistance heater. The thermal properties of the cell are then identified by calibrating an analytical thermal model with the experimental temperature data. A three-dimensional analytical model is developed for this purpose. It allows for simultaneous characterization of the cell anisotropy. The thermal properties are identified at 50% state of charge between 0 °C and 40 °C. Models with adiabatic and convection boundary conditions are compared and showed similar results. Overall, the values and tendencies agree with the literature. This non-destructive method can be directly applied to any pouch and prismatic cells, and adapted to cylindrical cell.

Keywords

Lithium-ion cell

Thermal characterization

Heat capacity

Anisotropic thermal conductivity

Analytical model

1. Introduction

1.1. Thermal issues of Lithium-ion battery

The growing popularity of hybrid and battery electric vehicles over the past ten years [1] makes the batteries a key factor for greener individual transports. Because of their high specific energy, lithium-ion (Li-ion) batteries are currently widely used to propel electric vehicles and are likely to be still in use in the years to come [2]. As a crucial aspect of vehicle propulsion, battery packs need to be correctly managed. Since the battery behavior is highly temperature dependent, thermal management plays especially a major role in battery operation.

Through experimental and modelling approaches, numerous works established how the operating temperature affects the batterie performances. Indeed, the temperature directly influences the battery capacity as high temperatures decrease the internal electrical resistance [3–5] and increase the open circuit voltage [4,6]. Thus, electric vehicles are expected to show weak performances and less range in wintry conditions [7–9]. The battery lifespan also suffers from extreme operating temperatures. Aging mechanisms in batteries result in loss of active material (lithium and/or electrode material) and increase of internal resistance, which respectively decreases the battery available capacity and power. Waldmann *et al.* [10] quantified the influence of temperature on aging rate by cycling commercial Li-ion cells. They identified the two main aging mechanisms and correlated an Arrhenius law to the respective aging rates. The growth of the Solid Electrolyte Interface (SEI) on the anode surface is caused by electrolyte decomposition and reaction with lithium [11–15]. Although SEI gradually thickens during the whole battery life, hot temperature accelerates its expansion. Conversely, lithium metal deposit on anode, known as lithium plating [10,12,16,17], is expecting to occur under harsh conditions: cold temperature, high charge rate, high state of charge and overcharging. In addition to inducing severe short-term degradation, the lithium metal is prone to grow as dendrites and break through the separator. This can potentially causes an internal short circuit and thermal runaway [18]. Other mechanisms such as manganese dissolution [19], mechanical degradation [20,21] and material corrosion and decomposition [12,21] can damage the battery. Mostly are triggered or worsened by hot temperatures.

Thermal management of battery packs is also destined to meet crucial issues such as fast charging and thermal runaway [22–24]. Predictive modelling is a powerful and essential tool to optimize the battery thermal management and to design new management technologies and strategies. Indeed, it allows to characterize the battery thermal behavior and to test various thermal management architectures without costly and time-consuming experimental campaigns [3,23,25,26]. However, thermal models require material specifications such as heat capacity and thermal conductivities. These data are usually not given by the battery manufacturers. To overcome this issue, numerous methods have been devised to estimate the thermal properties of batteries.

1.2. Thermal characterization of Lithium-ion batteries

1.2.1. Destructive methods

A battery is a composite material made of a stack of current collectors and electrochemical sheets (anode, cathode and separator) soaked with electrolyte. Because of their design, the batteries show an intrinsically anisotropic behavior. Therefore, two thermal conductivities are commonly distinguished: the conductivity perpendicular to the layers (through-plane conductivity, noted $\lambda_{\perp}$) and the conductivity parallel to the layers (in-plane conductivity, noted $\lambda_{\parallel}$).

Disassembling the batteries allows to directly measure the heat capacity of each sheet by calorimetry [27]. The global battery heat capacity is the average of the individual heat capacities weighted by the mass ratio. Similarly, the thermal conductivity of the battery can be calculated by measuring the thermal conductivity of each component. In this case, the conductivity is determined by imposing a thermal flux and measuring the temperature gradient [27–29]. Internal calorimetry and heat flow measurements are well suited to detailed modelling of the battery at the microscopic scale. They allow to reconstruct the stacked layers and to link the global behavior of the battery to the local behavior. In addition, Maleki *et al.* [27] showed that the electrolyte significantly increases the thermal conductivity compared to dried sheets. Richter *et al.* [29] confirmed these results on other batteries and showed the interest of compression. It is noteworthy that calorimetry can also be performed on a whole battery [30–34].

1.2.2. Non-destructive methods

The main drawback of the above-mentioned methods is that they destroy the battery. Non-destructive methods have been devised to be able to reuse the battery after the experiment. These methods are less costly and show especially useful for macroscopic modeling. They couple an experimental and a numerical approach. For a given experimental procedure, the temperature of the battery is measured. The experimental data are then used to calibrate a thermal model whose unknown parameters are the thermal capacity and the thermal conductivities of the battery.

Models of different kinds can be used for calibration. The analytical models give the exact solution of the heat equation. These models are fast-running and easy to use, but require simplification assumptions to be solvable (e.g., standard geometry, material homogeneity and steady boundary conditions). To the authors knowledge, only one-dimensional analytical models have been developed because of the solving complexity of multidimensional equations. They are still suitable for modeling pouch and prismatic cells [35,36] as well as cylindrical cell [33,37,38]. On the other hand, the numerical models use numerical methods such as the Finite Element Method (FEM) to solve partial differential equations. They are useful to represent the whole thermal field of a battery [37,39] and allow for complex modeling. Indeed, material inhomogeneities, dynamic loads and complex geometries and assemblies can be considered (e.g., Steinhardt *et al.* [40] used FEM to model the windings and the jelly roll gap of a prismatic cell). Compared to analytical models, the numerical models only give an approximation of the solution and involve high computational costs. Their precision and solving time strongly depend on the mesh size used for the spatial discretization. Because of that, simplified two-dimensional models are used for calibration purpose [41,42]. Finally, nodal thermal models are also popular in battery modeling because of their convenience. They are based on the mathematical analogy between electrical and thermal laws [43]. An equivalent electrical circuit is built, where a node represents an isothermal component (e.g., the cell core, the cell surface, or the external environment), and an electrical resistance represents a heat transfer. Since these models are not intended for detailed representation of the temperature field, one-dimensional models are often built [39,44]. Thermal resistances can however show useful to model the cell thermal behavior based on its microscopical structure [40,45].

Overall, the experimental procedure involves heating the battery and record the temperature rise at strategic locations, that is, locations such that a large thermal gradient can be measured based on the anisotropy direction being characterized. An external device can be used such as a heater [36,41] or an incandescent bulb [35]. A flexible heater is especially useful for the radial thermal characterization of cylindrical cells [37,38]. Other studies directly exploit the self-heating of the battery. An additional heat generation model [43,45] or a battery electrochemical model [42] must then be combined with the thermal model, which increases calibration uncertainties. The experimental setup is closely related to the thermal model and the calibration procedure. One-dimensional models only allow to determine the thermal conductivity of the cell along one dimension. Several experimental setups must then be designed to characterize the thermal anisotropy of a cell [37]. According to the present state of the art, only two-dimensional numerical models allow a simultaneous determination of the thermal properties of a battery, although they involve high computational costs and numerical errors.

1.3. Objective and structure of the paper

This paper aims at improving the analytical approach by developing a three-dimensional analytical thermal model. Only a single non-destructive experimental setup is therefore necessary to fully characterize the thermal anisotropy of the cell. As a result, both the experiment and the calibration time can be decreased. This method is applied to identify the battery thermal properties of a pouch cell at various temperatures. The paper is organized as follows. Section 2 describes the experimental setup and procedure. Section 3 develops the analytical model. Section 4 presents the calibration results and gives the thermal parameters of the battery as a function of temperature. Finally, section 5 discusses the relevance of the method.

2. Material and methods

2.1. Cell sample

A Li-ion pouch cell with NMC 622 ($LiNi_{0.6}Mn_{0.2}Co_{0.2}O_2$) cathode and graphite anode extracted from a commercial battery electric vehicle is used for this work. Its nominal capacity and nominal voltage are 60 Ah and 3.63 V respectively. The cell dimensions are 301 x 93 x 14 mm. The dimensions of the part containing the chemical material (including external packaging) are 263 x 93 x 14 mm. The mass of the cell was measured 888.8 g. The dimensions of the terminal were measured, and their material (thus their density) are known, which allows to estimate their mass. It can then be deduced that the volume containing the chemical material weighs 875.9 g, leading to a density of 2558 $kg.m^{-3}$.

2.2. Experimental setup

Beforehand, the cell has been set to 50% state of charge according to the capacity measured with a complete nominal discharge, which is performed at 30 A and 25 °C. The state of charge is fixed by conducting a nominal discharge from the fully charged state until the appropriate capacity has been discharged. The influence of the state of charge on the cell properties is outside the scope of this study, although it is supposed to be non-negligible. The state of charge of the battery will therefore be checked at the end of the experiment by measuring the open circuit voltage.

To prevent uncertainties linked to a heat generation model, the battery is heated by an external heater. The heat is emitted by a heater resistor that includes a printed circuit board on a thin copper plate with dimensions 30 x 30 x 0.2 mm. A heat flux sensor measures the actual heat transmitted from the resistor to the cell. This sensor also includes a copper plate with dimensions 30 x 30 x 0.4 mm. Its shape was purposely chosen to ensure better heat transfer. Furthermore, choosing identical area for the resistor and the sensor allows to perfectly align them and to obtain precise heat flux measurements. For the sake of eliminating contact resistance as well as evening out the heat over the heating area, thermal pad is intercalated to stick the resistor and the sensor together at the very center on the top of the cell. The resistor is powered by a DC generator. An inverting amplifier circuit has been built to amplify the sensor

output voltage so that it is compatible with the multimeter range. This assembly is represented on Figure 1. Table 1 gives the necessary specifications of the materials.

Twelve T-type thermocouples are attached to the cell by using their built-in patch and Kapton tape. They are indicated by yellow circles on Figure 2 (where the red square shows the heating area) and numbered from 1 to 12 for easier identification in the following sections. They have been suitably distributed on the cell surface to characterize the anisotropy of the cell, but close enough to the heat source because of the thermal inertia. The relative positions of the thermocouples are specified on Figure 2. The thermocouple No. 12, located at the furthest place, is also used to verify the validity of the model near the cell boundaries. These thermocouples will be used for the calibration of the thermal model. An additional thermocouple (No. 13) is directly attached in contact with the heating resistor for safety purpose.

The cell is snugly wrapped into several bubble wrap layers to thermally insulate it. It is placed in an insulating box built with extruded polystyrene panels of 50 mm thickness and 0.034 $W.m^{-1}.K^{-1}$ thermal conductivity. Fourteen additional T-type thermocouples are attached on the inner walls of this box (one on each corner and face center) and two more on the external side of the bubble wrap layers (opposite thermocouples No. 14 and 15).

The box is finally installed into a thermostatic chamber. By this way it is possible to vary the initial temperature condition. Since a renewed air flow keeps the chamber temperature constant, the insulating box acts as a barrier against the air flow and prevents convection cooling. The thermocouples are all connected to a thermocouple measurement box which transmits the data to an Analog to Digital Converter (ADC). The temperatures are read on a computer using CANalyzer software. The whole measurement chain is represented on Figure 3.

Table 1
Material specifications

Materials	**Technical data**	**Data source**
Heating resistor	Manufacturer: Captec Size: 30 x 30 x 0.2 mm Electrical resistance: $R_0 = 9.65\ \Omega$	Manufacturer
Heat flux sensor	Manufacturer: Captec Size: 30 x 30 x 0.4 mm Sensitivity: $\sigma_Q = 9.89.10^{-6} \pm 3\ \%\ V.m^2.W^{-1}$ The sensitivity is independent of temperature.	Manufacturer
Thermal pad	Manufacturer: RS PRO Thickness: 1 mm Thermal conductivity: 1.6 $W.m^{-1}.K^{-1}$ Temperature range: - 40 °C - +200 °C	Manufacturer
DC generator	Manufacturer and model: Aim-TTi, PL601-P Voltage range: 0 - 60 V Current range: 0 - 1.5 A	Manufacturer
Multimeter	Manufacturer and model: Fluke, 28-II DC Voltage range: 0.1 mV - 1000 V DC Voltage accuracy: 0.05% + 1 digit	Manufacturer
Amplifier circuit	Electrical resistance of resistors: $R_1 = 22\ k\Omega$, $R_2 = 1\ M\Omega$ Operational amplifier: Texas Instrument, LM258AP Offset: $\varepsilon_{op} = -1$ mV Gain: $\kappa_{op} = -45.9$	Measured

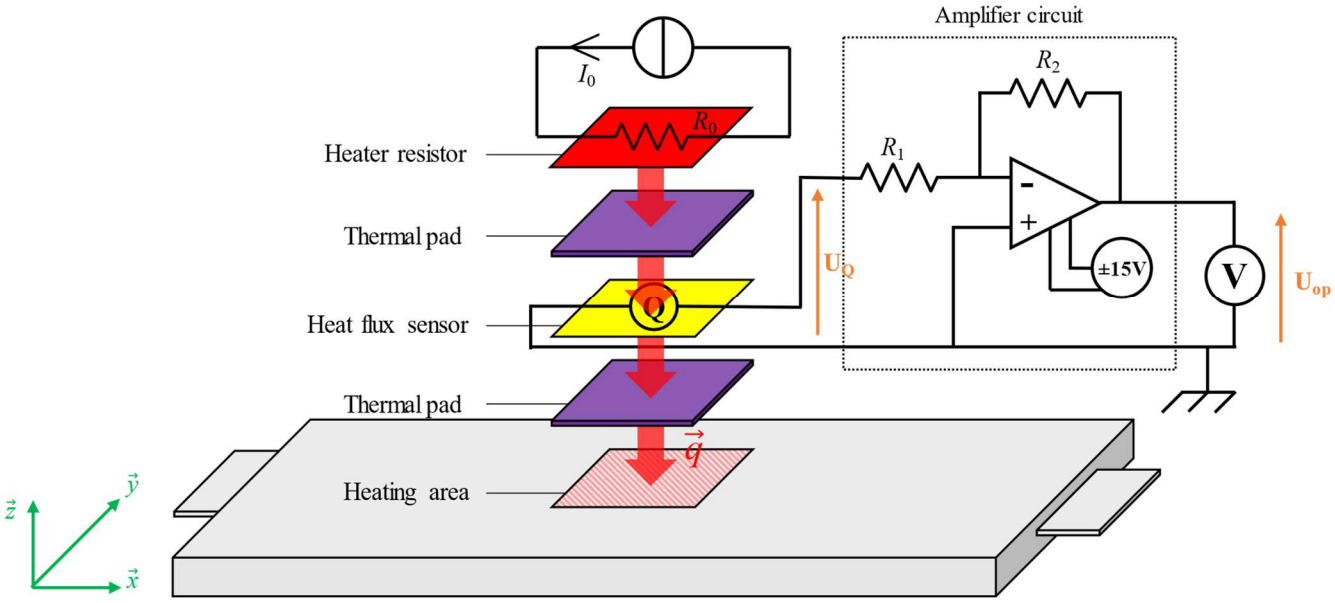

Figure 1 Schematic of the battery and electrical setup

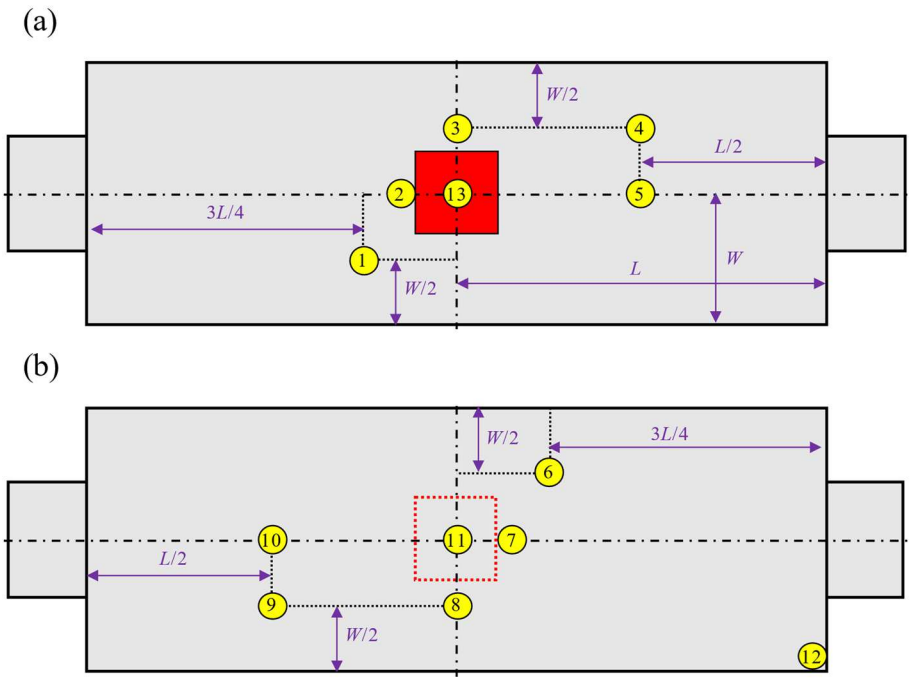

Figure 2 Repartition of the thermocouples on the battery surface (schematic reduced to scale)
(a) Top view, (b) Bottom view

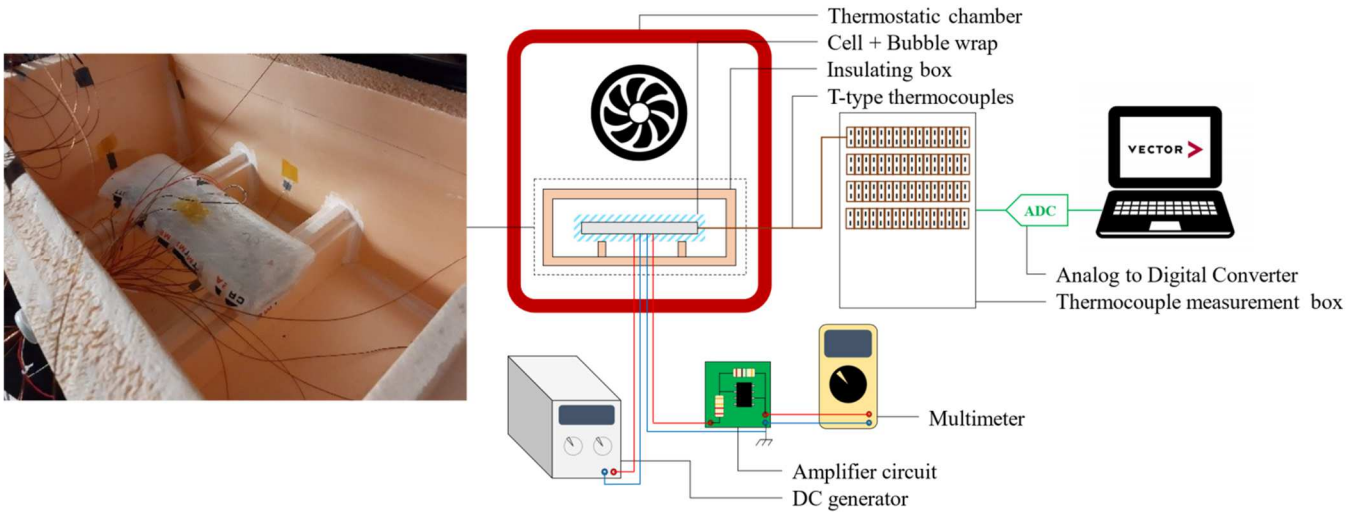

Figure 3 Schematic of the complete experimental setup

2.3. Experimental procedure

The experiment starts when the cell temperature equals the test temperature. The heater resistor is powered with the DC generator and the temperatures are automatically measured at 10 Hz frequency with CANalyzer. The resolution of the temperature measurement is 0.1 °C. The output voltage of the amplifier circuit is manually measured every minute with the multimeter. It should be noted that the sign of the output voltage of the heat flux sensor indicates the heat flux direction. The sensor is connected such that the sensor voltage U_Q and the amplifier voltage U_{op} are given by equation (1) and equation (2) respectively (see corresponding notations in Figure 1 and Table 1). According to Figure 1, U_Q therefore have negative values while U_{op} have positive values.

$$U_Q = \sigma_Q . \vec{q} . \vec{z} \quad (1)$$

$$U_{op} = \kappa_{op} . U_Q + \varepsilon_{op} \quad (2)$$

The experiment is interrupted as soon as thermocouple No. 2 (i.e. the closest one to the heating area) shows 5 °C temperature rise.

Experiments were conducted at 0 °C, 10 °C, 20 °C, 30 °C and 40 °C to characterize the temperature influence on the cell thermal properties. For a given test temperature, the test was performed at various input heat power to provide more experimental data. This is done by applying different input currents

with the DC generator: 300 mA, 320 mA, 340 mA, 360 mA and 380 mA. Assuming perfect adiabatic condition, the cell is subjected to heat power equal to the Joule losses of the resistor. Table 2 gives the tested currents as well as the expected heat powers and output voltages. Since low input current involves low input heat power and the end-of-test condition is temperature-triggered, it should be noted that the heating phase lasts longer with lower input current because the battery heats up more slowly.

Both the end-of-test condition and the input currents were chosen to limit the temperature rise and the temperature gradient inside the cell, so that the cell temperature stay close to the test temperature. This will be discussed in subsection 5.4.

The open circuit voltage of the cell is measured at the very beginning and the very end of the experiment with the multimeter (see Table 1). The open circuit voltage has been reduced by only 1 mV, which corresponds to less than 0.3% decrease in the state of charge. This proves that the state of charge is maintained throughout the experiment phase.

Table 2
Design of experiment and expected thermal flux

Input current [mA]	Power [W]	Surface power [kW.m^{-2}]	Heat flux sensor output voltage [mV]	Amplifier circuit output voltage [mV]
300	0.87	0.97	- 9.54	438
320	0.99	1.10	- 10.86	498
340	1.12	1.24	- 12.56	563
360	1.25	1.39	- 13.74	631
380	1.39	1.55	- 15.31	703

3. Theory

3.1. Assumptions

An analytical thermal model is used to fit the experimental data. Some assumptions are necessary to simplify its development:

- The cell terminals are not taken into account. This allows to reduce the cell geometry to a parallelepiped with dimensions 263 x 93 x 14 mm. This volume contains the cell chemical materials and packaging. By doing so, the heat sink due to the terminals is ignored.
- The abovementioned volume is an orthotropic and homogeneous material.
- All the cell surfaces, but the heating area, are adiabatic. This assumption highly depends on the thermal resistance offered by the bubble wrap and the insulating box.
- The heat flux $\vec{q}$ through the heating area is steady and uniform.

With respect to these assumptions and the cell assembly, the temperature field is expected to follow a symmetrical behavior. As a result, only a quarter of the cell needs to be modelled. This leads to consider the equivalent thermal problem depicted on Figure 4.

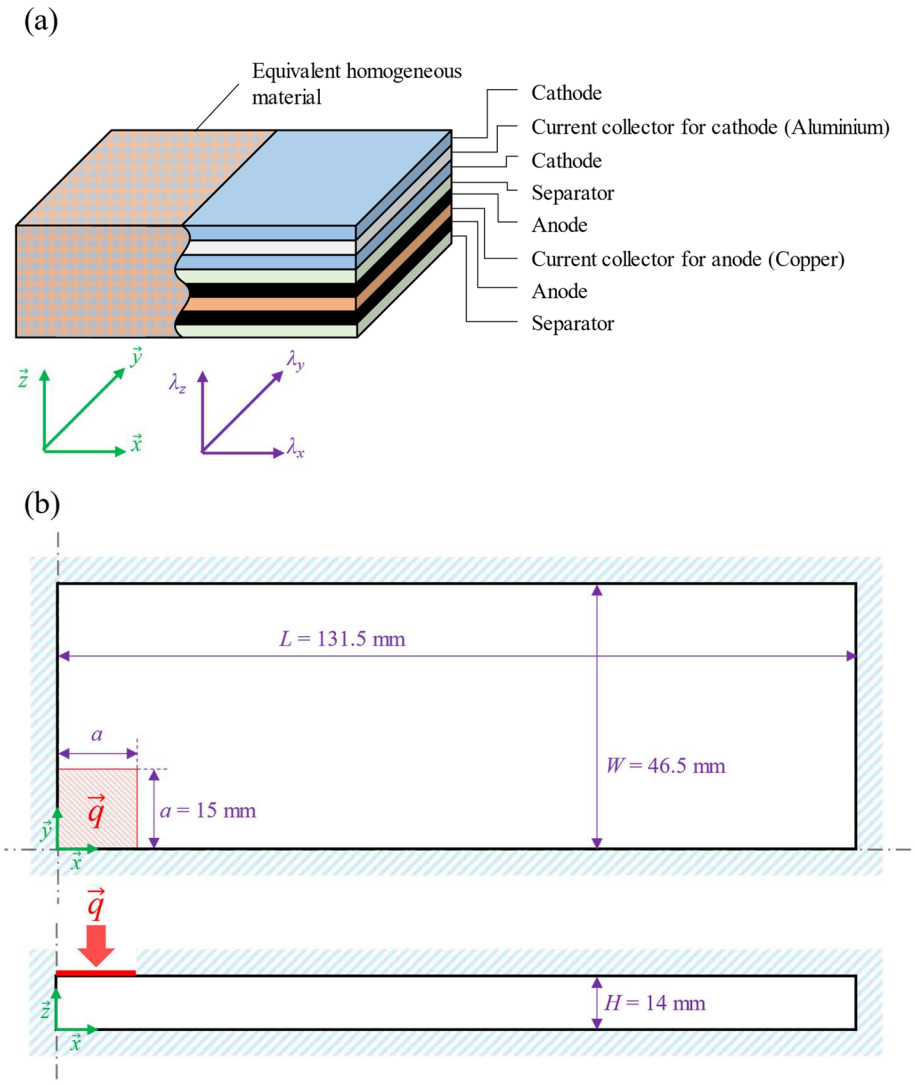

Figure 4 Cell modelling according to the assumptions (schematic reduced to scale).

(a) Homogeneity and anisotropy. An elementary cell stacking is represented to show that the three cartesian directions (x,y,z) coincide with the three orthotropic thermal conductivities (λ_x,λ_y,λ_z).
(b) Geometry, symmetry and boundary conditions. The slanting blue lines indicate adiabatic boundary conditions, i.e. null heat flux. The red area corresponds to the heating surface with uniform and steady heat flow $\vec{q}$.

3.2. Analytical model

3.2.1. Heat equation

Let $\theta(x,y,z,t)$ be the temperature rise of the cell. The analytical model involves determining the expression of θ by solving the three-dimensional heat equation:

$$\lambda_x.\frac{\partial^2\theta}{\partial x^2}+\lambda_y.\frac{\partial^2\theta}{\partial y^2}+\lambda_z.\frac{\partial^2\theta}{\partial z^2}-\rho.c_p.\frac{\partial\theta}{\partial t}=0 \quad (3)$$

where λ_i, ρ and c_p are the thermal conductivity along direction i, the density and the specific heat capacity of the cell respectively. The right-hand side of the equation is zero because there is no heat generation inside the cell. The uniformity hypothesis makes λ_i, ρ and c_p space independent. According to the end condition of the experiment, these parameters are also time independent.

Let introduce $\lambda = (\lambda_x.\lambda_y.\lambda_z)^{1/3}$ and $\Lambda_i = (\lambda/\lambda_i)^{1/2}$ to apply the following variable change:

$$(x\,,y\,,z)\mapsto(X\,,Y\,,Z)=\left(\Lambda_x.x\,,\Lambda_y.y\,,\Lambda_z.z\right) \quad (4)$$

Equation (3) is rewritten with this new set of variables:

$$\frac{\partial^2\theta}{\partial X^2}+\frac{\partial^2\theta}{\partial Y^2}+\frac{\partial^2\theta}{\partial Z^2}-\frac{\rho.c_p}{\lambda}.\frac{\partial\theta}{\partial t}=0 \quad (5)$$

The boundary conditions are:

$$-\frac{\lambda}{\Lambda_z}.\frac{\partial\theta}{\partial Z}\Big|_{\substack{Z=\Lambda_z.H \\ \{0\le x\le a\}\cap\{0\le y\le a\}}} = -\|\vec{q}\| = -Q \tag{6}$$

$$\frac{\partial\theta}{\partial Z}\Big|_{\substack{Z=\Lambda_z.H \\ \{\Lambda_x.a<X\le\Lambda_x.L\}\cup\{\Lambda_y.a<Y\le\Lambda_y.W\}}} = \frac{\partial\theta}{\partial Z}\Big|_{Z=0} = \frac{\partial\theta}{\partial X}\Big|_{X=0} = \frac{\partial\theta}{\partial X}\Big|_{X=\Lambda_x.L} = \frac{\partial\theta}{\partial Y}\Big|_{Y=0} = \frac{\partial\theta}{\partial Y}\Big|_{Y=\Lambda_y.W} = 0 \tag{7}$$

As the experiment starts in a thermal equilibrium state, the initial condition is given by:

$$\lim_{t\to 0}\theta = 0 \tag{8}$$

The thermal problem is similar to the experiment conducted by Zhang *et al.* [41], who however used a computationally costly two-dimensional finite element model to solve the problem. An analytical thermal model is then adopted to decrease computational costs and increase accuracy. To the authors knowledge, the analytical models developed for battery thermal characterization deal with only one spatial dimension and uniform boundary conditions [33,35–38]. The method presented in this paper improves the analytical approach as it involves a three-dimensional analytical model with discontinuous boundary conditions to characterize the anisotropy of the battery with a single experiment.

3.2.2. Eigenfunctions and integral transform

The first step involves finding the eigenvalues and eigenfunctions by solving the homogeneous problem. The Fourier method, also known as the separation of variables method, is applied. The space variables X, Y, Z and the time variable t are separated by introducing the functions ψ, φ, φ_X, φ_Y and φ_Z:

$$\theta(X,Y,Z,t) = \varphi(X,Y,Z).\psi(t) = \varphi_X(X).\varphi_Y(Y).\varphi_Z(Z).\psi(t) \tag{9}$$

Following the Fourier method shows that the solution of the homogeneous problem is a linear combination of the eigenfunctions $\{\varphi_{nkp}, (n,k,p)\in\mathbb{N}^3\}$:

$$\theta_0(X,Y,Z,t) = \sum_{n\ge 0}\sum_{k\ge 0}\sum_{p\ge 0} K_{n,k,p}.\varphi_{n,k,p}(X,Y,Z).e^{\frac{-\lambda.\delta_{n,k,p}^2}{\rho.c_p}.t} \tag{10}$$

The eigenfunctions are found through the boundary conditions. Each eigenfunction φ_{nkp} is the product of the thee eigenfunctions $\varphi_{X,n}$, $\varphi_{Y,k}$ and $\varphi_{Z,p}$ respectively related to the three space variables X, Y and Z:

$$\varphi_{nkp}(X,Y,Z) = \varphi_{X,n}(X).\varphi_{Y,k}(Y).\varphi_{Z,p}(Z) = \cos\left(\frac{n.\pi}{\Lambda_x.L}.X\right).\cos\left(\frac{k.\pi}{\Lambda_y.W}.Y\right).\cos\left(\frac{p.\pi}{\Lambda_z.H}.Z\right) \tag{11}$$

δ_{nkp} is the eigenvalue associated to φ_{nkp} and can be seen as the Euclidean norm of three eigenvalues α_n, β_k and γ_p respectively related to $\varphi_{X,n}$, $\varphi_{Y,k}$ and $\varphi_{Z,p}$:

$$\delta_{nkp} = \sqrt{\alpha_n^2 + \beta_k^2 + \gamma_p^2} = \sqrt{\left(\frac{n.\pi}{\Lambda_x.L}\right)^2 + \left(\frac{k.\pi}{\Lambda_y.W}\right)^2 + \left(\frac{p.\pi}{\Lambda_z.H}\right)^2} \tag{12}$$

It should be noted that the eigenfunctions are orthogonal. This allows to define the following integral transform of θ_0 of order $\{n,k,p\}$:

$$\overline{\theta_0}_{nkp}(t) = \int_0^{\Lambda_z.H}\int_0^{\Lambda_y.W}\int_0^{\Lambda_x.L} \theta_0.\varphi_{nkp}(X,Y,Z).dX.dY.dZ \tag{13}$$

The above equation combined with equation (9) is used to determine the coefficients K_{nkp}. This gives the homogeneous solution as well as the inversion formula of the integral transform:

$$\theta_0(X,Y,Z,t) = \sum_{n\geq 0}\sum_{k\geq 0}\sum_{p\geq 0} \frac{\varphi_{nkp}(X,Y,Z)}{\int_0^{\Lambda_z.H}\int_0^{\Lambda_y.W}\int_0^{\Lambda_x.L}\varphi_{nkp}^2(X,Y,Z).dX.dY.dZ}.\overline{\theta_0}_{n,k,p}(t) \tag{14}$$

3.2.3. General solution

Equation (5) can be multiplied by $\varphi_{n,k,p}$ and integrated over the volume. Then, successively applying the Green's second identity and equation (13) turns equation (5) into a time-dependent differential equation:

$$\delta_{nkp}^2.\bar{\theta}_{nkp} - Q.\frac{\Lambda_z}{\lambda}.\int_0^{\Lambda_x.a}\int_0^{\Lambda_y.a}\varphi_{nkp}(X,Y,Z=\Lambda_z.H).dY.dX + \frac{\rho.c_p}{\lambda}.\frac{\partial\bar{\theta}_{nkp}}{\partial t} = 0 \tag{15}$$

Solving equation (15) and applying the reverse integral transform from equation (14) gives the analytical formula of the temperature rise inside the cell:

$$\theta(X,Y,Z,t) = F_{000}.\frac{Q.\Lambda_Z.J_{000}^{heater}}{\rho.c_p} + \sum_{\substack{n\geq 0\\ k\geq 0\\ p\geq 0\\ \text{n+k+p}\neq 0}} F_{nkp}(X,Y,Z).\frac{Q.\Lambda_Z.J_{nkp}^{heater}}{\gamma.\delta_{nkp}^2}.\left(1-e^{-t/\tau_{nkp}}\right) \quad (16)$$

where:

$$F_{nkp}(X,Y,Z) = \frac{\varphi_{nkp}(X,Y,Z)}{\int_0^{\Lambda_z.H}\int_0^{\Lambda_y.W}\int_0^{\Lambda_x.L}\varphi_{nkp}^2(X,Y,Z).dX.dY.dZ} \quad (17)$$

$$J_{nkp}^{heater} = \int_0^{\Lambda_x.a}\int_0^{\Lambda_y.a}\varphi_{nkp}(X,Y,Z=\Lambda_z.H).dY.dX \quad (18)$$

$$\tau_{nkp} = \frac{\rho.c_p}{\lambda.\delta_{nkp}^2} \quad (19)$$

Since adiabatic boundary conditions were considered, the temperature keeps rising over time inside the cell. Instead of a steady state, the model contains an asymptotic affine behavior which is space independent. If the model assumptions about the boundary conditions are correct, it can be demonstrated that this affine component corresponds to the mean temperature of the cell [37].

3.2.4. Model with convection boundary conditions

Although the experiment has been designed with adiabatic boundary conditions, an alternative model is proposed to take into account potential heat losses through the insulation. The parameter $h_{cell\text{-}air}$ is introduced as the heat transfer coefficient between the cell surface and the air of the thermostatic chamber and is used to model an equivalent convection boundary condition on the cell surfaces. $h_{cell\text{-}air}$ is assumed to be homogeneous on all the cell surfaces.

These new boundary conditions introduce new eigenfunctions described by equation (20):

$$\varphi_{nkp}(X,Y,Z) = \cos(\alpha_n.X).\cos(\beta_k.Y).\left[\gamma_p.\cos(\gamma_p.Z) + \frac{\Lambda_z.h_{cell-air}}{\lambda}.\sin(\gamma_p.Z)\right] \quad (20)$$

The eigenvalues α_n, β_k and γ_p are the strictly positive roots of equation (21), (22) and (23) respectively:

$$\alpha \mapsto \alpha.\tan(\alpha.\Lambda_x.L) - \frac{\Lambda_x.h_{cell-air}}{\lambda} \tag{21}$$

$$\beta \mapsto \beta.\tan\left(\beta.\Lambda_y.W\right) - \frac{\Lambda_z.h_{cell-air}}{\lambda} \tag{22}$$

$$\gamma \mapsto \tan(\gamma.\Lambda_z.H) - \frac{2.\frac{\Lambda_z.h_{cell-air}}{\lambda}.\gamma}{\gamma^2 - \left(\frac{\Lambda_z.h_{cell-air}}{\lambda}\right)^2} \tag{23}$$

The analytical solution of this problem is given by the following equation:

$$\theta(X,Y,Z,t) = \sum_{\substack{n>0\\k>0\\p>0}} F_{nkp}(X,Y,Z).\frac{Q.\Lambda_z.J_{nkp}^{heater}}{\lambda.\delta_{n,k,p}^2}.\left(1 - e^{-t/\tau_{nkp}}\right) \tag{24}$$

4. Results

4.1. Heat power

To illustrate the behavior of the heater resistor, Figure 5 displays the voltage rise measured at the terminals of the amplifier circuit for the test performed at 20 °C and 380 mA. The heater behaves like a first order system. The time constant is measured about 30 s. The voltage does not tend towards a steady value but decreases progressively after reaching a maximum value. A zoom highlights the curve decrease in Figure 5. Table 3 gives the total loss at the end of each experiment relative to actual steady input (i.e. if the power remains at its maximum). Regardless of the operating condition, the total loss never exceeds 1%. This supports the hypothesis of a steady thermal input.

The heater produces heat by Joule effect. With adiabatic boundary conditions, all the heat should be transferred to the cell. However, the maximum measured voltage is lower than the expected value (see

Table 2) from about 6% at 0 °C up to 9% at 40 °C. Since these values are outside the uncertainty range of the heat flux sensor, it can be inferred that part of the heat spreads through the insulation. The validity of the adiabatic boundary condition must then be assessed and will be discussed in subsection 5.5.

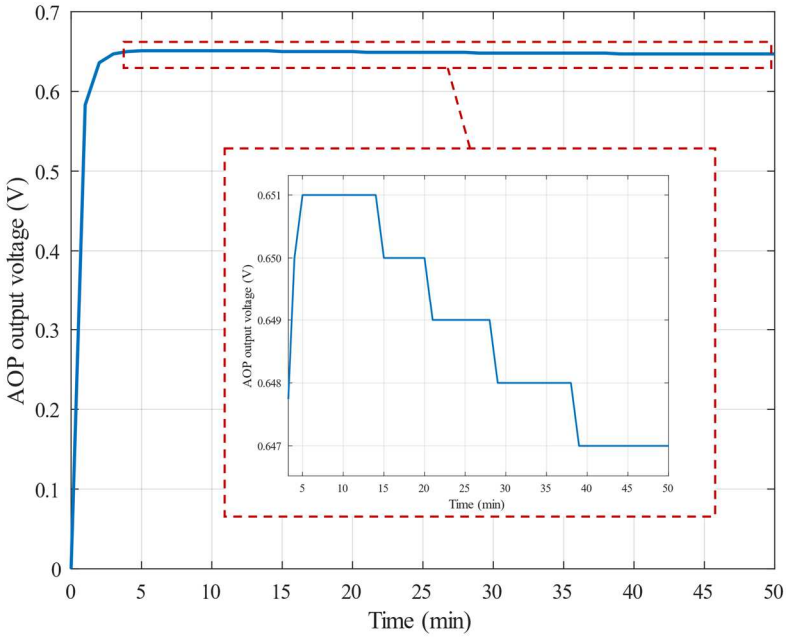

Figure 5 Output voltage from the amplifier circuit (test temperature: 20 °C, input current: 380 mA)

Table 3
Deviation of the heat fux steadiness hypothesis. For each operating point, the table gives the total loss of heat power Q at the end of each test relative to actual steady condition.

	Test temperature				
Input current	**0 °C**	**10 °C**	**20 °C**	**30 °C**	**40 °C**
300 mA	- 0.92%	- 0.58%	- 0.38%	- 0.76%	- 0.84%
320 mA	- 0.45%	- 0.66%	- 0.57%	- 0.72%	- 0.47%
340 mA	- 0.60%	- 0.41%	- 0.56%	- 0.42%	- 0.89%
360 mA	- 0.45%	- 0.39%	- 0.42%	- 0.41%	- 0.29%
380 mA	- 0.40%	- 0.59%	- 0.34%	- 0.25%	- 0.29%

4.2. Temperature profile

Figure 6 displays the temperature rise measured by the thermocouples attached to the cell for the test performed at 20 °C and 380 mA. The curves show steps because of the relatively low resolution of the temperature measurement (0.1 °C) compared to the high frequency measurement (10 Hz). At first glance,

the temperature seems to follow a linear asymptotic behavior after a transient phase. The slope of the linear part also seems space independent, which would agree with theoretical section. Regarding the temperature raw values, it is evident that the closer the thermocouples are to the heating area, the higher the temperature rise. This temperature gradient proves that this experiment allows to characterize the thermal anisotropy of the cell.

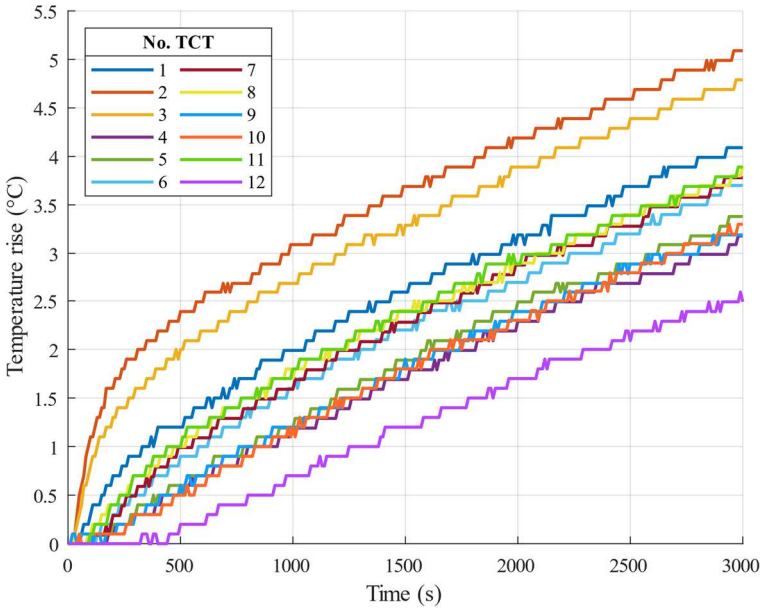

Figure 6 Temperature rise on the cell surface (test temperature: 20 °C, input current: 380 mA)

4.3. Model calibration

4.3.1. Methodology

The calibration of the experimental data is done with a least square method by using the function *lsqcurvefit* in MATLAB. The calibration parameters are the specific heat capacity c_p and the thermal conductivities λ_x, λ_y and λ_z of the cell. According to the model hypotheses and the geometry (see Figure 4), it can be considered $\lambda_x = \lambda_y = \lambda_{||}$ (in-plane conductivity) and $\lambda_z = \lambda_{\perp}$ (though-plane conductivity). Thus, the number of calibration parameters is reduced, which increases accuracy.

For each test temperature, the experimental data of all thermocouples and all input currents are fitted altogether to the model. This is necessary to avoid scattering of the calibration parameter, as they are independent of the input heat power. The experimental data are uniformly sampled to 200 points to

shorten the calibration time. For the same purpose, the analytical model is approximated by finite sums. Only the first fifty eigenvalues are considered for each eigenfunction.

Two calibration methods are proposed in the following subsections. Firstly, the measured data are considered only for a restricted experiment duration so that the adiabatic boundary conditions are still relevant. Then, the model with convection boundary conditions is calibrated for the whole experiment. This adds the thermal resistance $h_{cell\text{-}air}$ as a calibration parameter.

4.3.2. Model with adiabatic boundary conditions

It has been showed in subsection 4.1 that part of the power generated by the heater spreads through the insulation, which means that adiabatic conditions are not met. However, there should be an experiment duration limit during which heat losses can be neglected and adiabatic boundary conditions are relevant. This limit is determined by measuring the temperature of the thermocouple located on the bubble wrap under the cell and checking when the temperature rise becomes significant. By arbitrarily choosing a limit of 0.5 °C, the duration limit of 8 minutes is identified.

The calibration is then performed by taking only the first 8 minutes of each experiment. Since the analytical model requires a constant heat power as input, the heat power measured with the heat flux sensor is averaged from when it first reaches 95% of its maximum value to the end of the experiment.

After calibration, the root main square errors (RMSe) are calculated in Table 4 for each operating point while the fitted thermal parameters are given in Table 5. The RMSe values are very low but should be considered relatively with the temperature rise of the cell. Indeed, the temperature rise is low as well (only a few 0.1 °C for some thermocouples) due to the restricted experiment time. Thus, no relevant conclusion could be done about the calibration accuracy.

Table 4
Root mean square error (°C) between the experimental data and the model (adiabatic boundary conditions, 8-minute experiment).

	Test temperature				
Input current	**0 °C**	**10 °C**	**20 °C**	**30 °C**	**40 °C**

300 mA	0.09	0.08	0.07	0.08	0.08
320 mA	0.09	0.08	0.08	0.08	0.09
340 mA	0.09	0.09	0.09	0.09	0.09
360 mA	0.10	0.09	0.10	0.11	0.10
380 mA	0.10	0.11	0.11	0.11	0.11

Table 5
Calibration of the thermal parameters c_p, $\lambda_{\parallel}$ and $\lambda_{\perp}$ of the cell (adiabatic boundary condition, 8-minute experiment).

	Test temperature				
	0 °C	**10 °C**	**20 °C**	**30 °C**	**40 °C**
Specific heat capacity c_p ($J.kg^{-1}.K^{-1}$)	1096	1151	1159	1190	1203
In-plane thermal conductivity $\lambda_{\parallel}$ ($W.m^{-1}.K^{-1}$)	20.1	20.3	19.9	20.0	21.1
Through-plane thermal conductivity $\lambda_{\perp}$ ($W.m^{-1}.K^{-1}$)	1.33	1.24	1.25	1.22	1.17

4.3.3. Model with convection boundary conditions

An 8-minute experiment does not completely avoid heat losses and involves more calibration uncertainties since the temperature rise is lower. By considering a global heat transfer coefficient between the cell and the air of thermostatic chamber (see subsection 3.2.4), the resulting analytical model should be consistent for the whole experiment and provide more reliable results. Since these convection boundary conditions are also applied on the heating area of the cell, the total Joule losses of the heater (see 3rd column in Table 2) are taken as input heat power for physical consistency.

At 20 °C test temperature and 380 mA input current, Figure 7 shows the measured and modelled temperature for the twelve thermocouples after calibration. The analytical model perfectly fits the experimental data for every thermocouple. As a result, applying a global heat transfer coefficient is relevant to model the heat losses. The accuracy of the calibration is quantified in Table 6 by the RMSe values, which are about only 0.1 °C for every operating point. Compared to the global temperature rise of the cell, the calibration accuracy can be established. Thus, the calibrated thermal parameters should be physically consistent. These parameters are gathered in Table 7. The heat transfer coefficient shows a decreasing linear behavior between 10 °C and 40 °C, while the values are the same at 0 °C and 10 °C. The behavior of the other parameters is discussed in the following subsection and compared with the other model.

Table 6
Root mean square error (°C) between the experimental data and the model (convection boundary conditions, full experiment).

	Test temperature				
Input current	**0 °C**	**10 °C**	**20 °C**	**30 °C**	**40 °C**
300 mA	0.11	0.12	0.09	0.11	0.12
320 mA	0.11	0.11	0.10	0.10	0.15
340 mA	0.13	0.11	0.12	0.12	0.11
360 mA	0.12	0.12	0.11	0.13	0.11
380 mA	0.11	0.13	0.12	0.12	0.12

Table 7
Calibration of the thermal parameters c_p, $\lambda_{\parallel}$ and $\lambda_{\perp}$ of the cell (convection boundary conditions, full experiment).

	Test temperature				
	0 °C	**10 °C**	**20 °C**	**30 °C**	**40 °C**
Specific heat capacity c_p ($J.kg^{-1}.K^{-1}$)	1084	1101	1119	1137	1165
In-plane thermal conductivity $\lambda_{\parallel}$ ($W.m^{-1}.K^{-1}$)	19.4	19.8	19.6	19.9	20.7
Through-plane thermal conductivity $\lambda_{\perp}$ ($W.m^{-1}.K^{-1}$)	1.37	1.32	1.29	1.28	1.22
Heat transfer coefficient $h_{cell\text{-}air}$ ($W.m^{-2}.K^{-1}$)	2.72	2.72	2.95	3.15	3.39

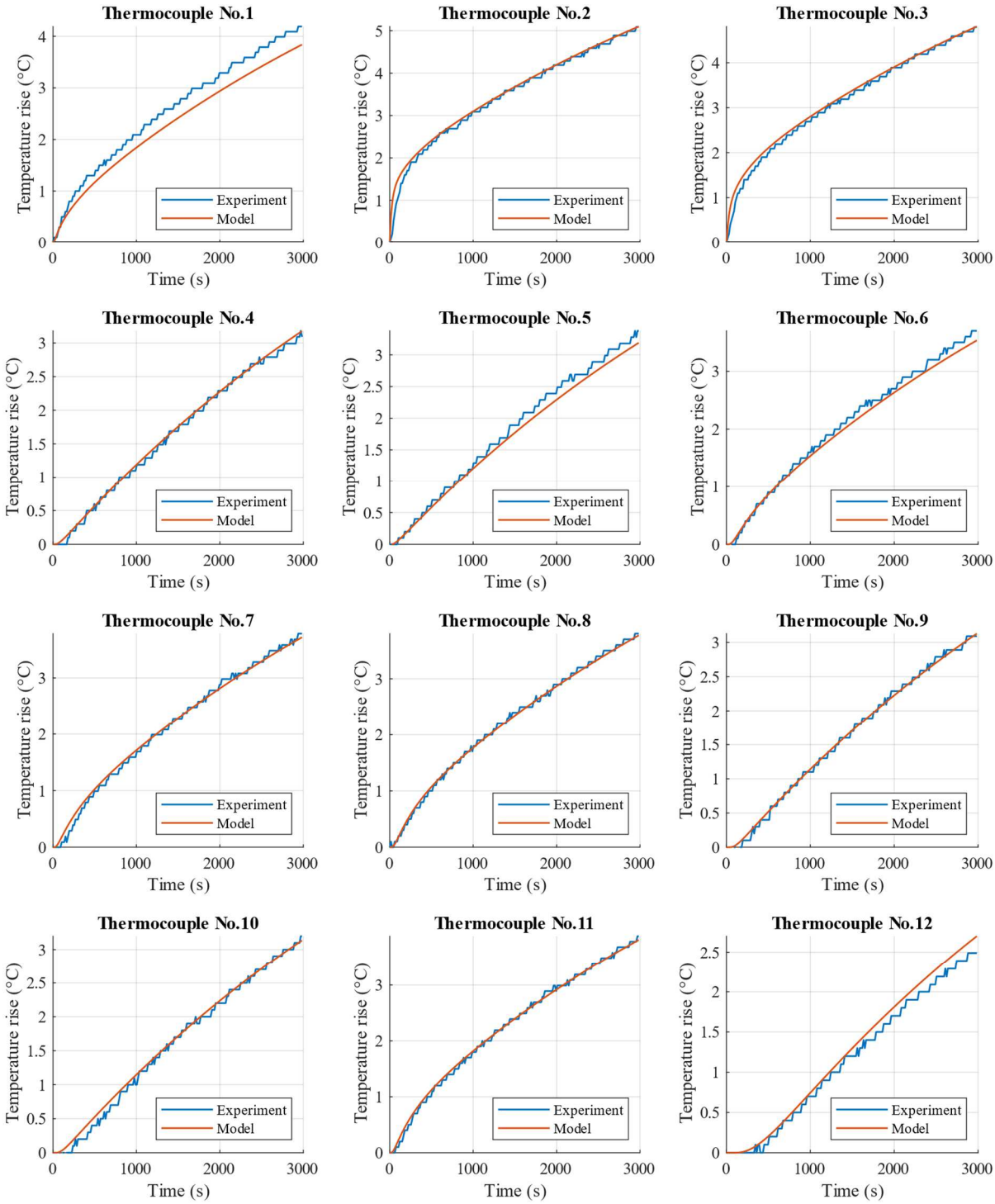

Figure 7 Measured and modelled temperature rise (test temperature: 20 °C, input current: 380 mA)

4.3.4. Comparison

The thermal parameters from Table 5 and Table 7 are displayed in Figure 8 as a function of temperature. Interpolation curves have been added to underline the global behavior of the parameters. The specific heat capacity and the through-plane thermal conductivity appear to follow a linear behavior for

the considered temperature range, while a second-order polynomial fits the in-plane conductivity better. It should be noticed that the interpolation error is significantly smaller for the values obtained with convection boundary conditions.

The interpolation curves also show that there is an overall difference between the two models. Table 8 gives the relative errors between the thermal parameters. On average, the specific heat capacity and the in-plane thermal conductivity are respectively only 3.4% and 2.0% higher with adiabatic boundary conditions compared to convection boundary conditions. Conversely, the through-plane thermal conductivity is lower by only 4.0%. This shows that both models give similar results and that the analytical model with adiabatic boundary conditions can give realistic values even if the model assumptions are not perfectly met.

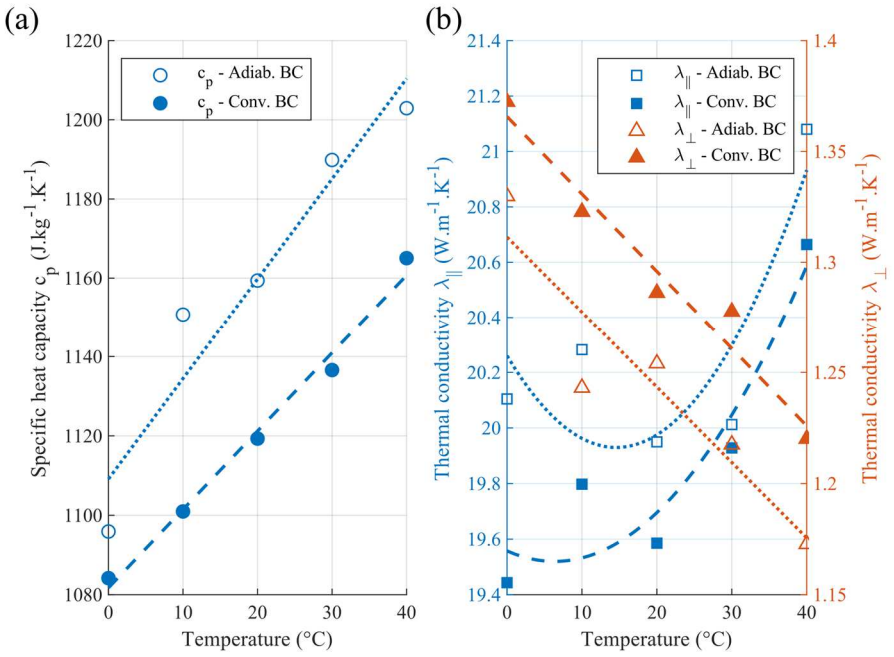

Figure 8 Thermal properties of the cell vs. temperature, obtained with both models ("BC" stands for "boundary conditions"). The dotted and dashed curves are the interpolation curves associated with the adiabatic and convection boundary conditions respectively. (a) Specific heat capacity. (b) Thermal conductivities.

Table 8
Relative error between the thermal parameters c_p, $\lambda_{\parallel}$ and $\lambda_{\perp}$ obtained with both models.

	Test temperature				
	0 °C	**10 °C**	**20 °C**	**30 °C**	**40 °C**
Specific heat capacity c_p	1.1%	4.5%	3.6%	4.7%	3.3%
In-plane thermal conductivity $\lambda_{\parallel}$	3.4%	2.4%	1.9%	0.4%	2.0%
Through-plane thermal conductivity $\lambda_{\perp}$	-3.1%	-6.0%	-2.5%	-4.7%	-3.9%

5. Discussion

5.1. Comparison with results of other studies

The specific heat capacities determined in this work are quite similar to those reported in the literature for NMC cells [36,39,42,44]. The increasing linear behavior is also consistent with other Li-ion chemistries [34,36,38,39]. Despite the values of the thermal conductivities show no significant correlation with other studies, the difference of at least one order of magnitude between the in-plane and the though-plane conductivity reflects the results of other works [33,37,39,41,42]. The decreasing linear behavior of the through-plane thermal conductivity also mirrors the results of various studies [38,40,45] but contradicts with the work of Sheng *et al.* [36] who found increasing tendencies for the cells they tested. The authors found no data about the in-plane thermal conductivity as a function of temperature which would corroborate or contest the present work.

No literature can validate the values found for the heat transfer coefficient. Indeed, it combines several media (air and extruded polystyrene) and heat transfers (conduction and convection). However, a global increasing behavior was expected when looking at the thermal conductivities of air and extruded polystyrene. The gap between the expectations and the actual result could be due to both measurement and calibration uncertainties.

5.2. Material and experiment

The setup presented in this work requires no overpriced material or material which is not commonly found in most laboratories.

The method is easily feasible and non-destructive. This is crucial to successively test several configurations and compare results without manufacturing bias. However, the experiment can be quite time consuming because of the rest phase after each operating point. The rest phase took several hours and was necessary to meet the initial condition of the model. However, this time can be reduced by opening the insulating box inside the thermostatic chamber to increase the cell cooling. With the chosen end-of-experiment condition, the heating time depended on the heat power. It could last more than 2 hours at 380 mA input current. This phase can be optimized by choosing appropriate and sufficient operating conditions.

Additionally, the whole experiment can be automated to further decrease the experiment duration. Indeed, the input current could be set on and off according to temperature initial and final conditions. This would allow to perform a continuous experiment.

The method allows to simultaneously identify the thermal parameters for different cell temperatures by only adjusting the temperature inside the thermostatic chamber. In order to study the influence of the state of charge, it is mandatory to undo the setup before adjusting the state of charge of the cell.

Finally, it should be noted that the experiment was conducted with the same location and area of the heat source. In this paper, the heat source is centered on one of the large surfaces of the pouch cell, so that the temperature field is symmetrical, and the heat is more evenly spread within the cell. Moving the heat source would increase the maximum temperature gradient inside the cell and unbalance the heat distribution. This would therefore question the dependance of the identified parameters to the temperature (see section 5.4). A similar issue arises when modifying the size of the heat source. Increasing it decreases the temperature gradient inside the cell, which allows a more uniform distribution of heat but decreases the accuracy of the calibration. The cell could also be heated by using its internal heat source during operation. Doing so involves volume heating instead of surface heating, and alters the boundary conditions since the terminals and power cables represent a significant heat sink. Furthermore, the applied current profile needs to be carefully chosen to avoid high deviations of the state of charge.

5.3. Modeling assumptions

Compared to numerical and nodal models, the analytical model involves no solving error. The errors only come from the modeling assumptions.

Because of measurement uncertainties when measuring the cell weight and dimensions, inaccuracies can be expected for the cell density. These uncertainties are supposed to be negligible compared to other sources of inaccuracy, especially the temperature measurement.

The cell terminals are very thin and should involve only very little influence as a heat sink. The very low calibration errors (see Table 4 and Table 6) validate this assumption and justifies $\lambda_x = \lambda_y = \lambda_{\parallel}$. The adopted geometrical representation of the cell is therefore relevant.

The homogeneity assumption is supported by the cell structure. Indeed, a pouch cell is a stack of several elementary cells (see Figure 4.(a)) that is wrapped in a thin and flexible packaging which perfectly fits the structure shape. Given that the thickness of the electrochemical sheets is in the microscopical range, the battery can then be macroscopically considered as a global parallelepiped material. This especially justifies the uniformity of c_p, $\lambda_{\parallel}$ and $\lambda_{\perp}$. The orthotropic behavior of the cell also comes from the staking structure. Only local irregularities and detachment of the packaging could affect these assumptions.

The uniformity of the heat flux is assured by the material, especially the thermal pad. Applying the desired heat flux with the heater resistor is not instantaneous and shows no strict convergence. However, the short time constant of the heat flux as well as the reported voltage from the heat flux sensor (see Table 3) allow to validate the heat flux steadiness assumption.

5.4. Temperature dependance

Because the influence of temperature was studied, the thermal gradient and the temperature rise of the cell needed to be limited. Table 9 and Table 10 respectively give the average temperature and the maximum temperature gradient inside the cell at the end of the heating phase. All these values have been estimated with the model with convection boundary conditions and by applying the thermal parameters

determined in subsection 4.3.3. The average temperature does not exceed 4 °C. Due to the end condition for the experiment, a lower input current involves a longer duration of the heating phase and a higher average temperature. Table 10 shows that there is no more than 5 °C difference inside the cell and that the gradient decreases with decreasing input heat flux. From these values, it can then be considered that the thermal parameters obtained in subsection 4.3 are indeed related to the operating temperature. The temperature dependence can be refined by decreasing the experiment time.

Table 9
Average temperature of the cell (°C) estimated from the analytical model and thermal parameters from subsection 4.3.3.

	Test temperature				
Input current	**0 °C**	**10 °C**	**20 °C**	**30 °C**	**40 °C**
300 mA	4.02	4.10	3.62	3.48	3.62
320 mA	4.26	3.91	3.75	3.79	3.59
340 mA	4.19	3.84	3.84	3.71	3.62
360 mA	3.83	3.55	3.42	3.48	3.33
380 mA	3.64	3.47	3.34	3.48	3.17

Table 10
Temperature gradient inside the cell (°C) estimated from the analytical model and thermal parameters from subsection 4.3.3.

	Test temperature				
Input current	**0 °C**	**10 °C**	**20 °C**	**30 °C**	**40 °C**
300 mA	3.16	3.18	3.23	3.20	3.20
320 mA	3.59	3.61	3.67	3.64	3.63
340 mA	4.05	4.06	4.13	4.10	4.09
360 mA	4.53	4.55	4.62	4.59	4.58
380 mA	5.04	5.06	5.14	5.10	5.09

5.5. Validity of the adiabatic boundary conditions

The experimental setup described in Figure 3 was inadequate to efficiently insulate the cell. It was demonstrated that including convection boundary conditions in the analytical model proved accurate and gave reliable results. However, subsection 4.3.4 showed that the model with adiabatic boundary conditions is not completely inaccurate.

The comparison between both models is further quantified in Table 11. The table gives the maximum temperature error between the models when using the same thermal parameters (the values from Table 7

are used for this purpose). The cell temperature is only calculated at the thermocouple location (see Figure 2) and after 8 minutes of heating to match the experimental conditions. It should be mentioned that the maximum error is dominated by thermocouples No. 2 and 3. In other words, the error increases close to the heat source. The temperature difference slightly increases with increasing heat power and increasing temperature. This behavior is linked by both the temperature rise and the heat transfer coefficient. The difference can reach 0.15 °C, which is very close to the measurement resolution of the thermocouples (0.1 °C). With the experimental setup used in this study, considering 8 minutes of heating is then acceptable to apply adiabatic boundary conditions.

The validity of adiabatic boundary conditions strongly depends on the thermal insulation combined with the heating time. It should be remembered that the temperature rise must be high enough to reduce the measurement and calibration uncertainties. Conversely, effective thermal insulation is not necessary if convection boundary conditions are modeled. With this model, the heat transfer coefficient must also be calibrated, which adds calibration uncertainties.

Table 11
Maximum error (°C) between the two models after 8 minutes.

	Test temperature				
Input current	**0 °C**	**10 °C**	**20 °C**	**30 °C**	**40 °C**
300 mA	0.08	0.07	0.08	0.10	0.10
320 mA	0.08	0.09	0.10	0.11	0.11
340 mA	0.09	0.10	0.12	0.12	0.13
360 mA	0.10	0.12	0.12	0.14	0.14
380 mA	0.10	0.14	0.16	0.15	0.15

6. Conclusion

The method presented in this paper allows to identify the thermal material properties of a battery. The specific heat capacity, the in-plane and the through-plane thermal conductivities were simultaneously determined with a non-destructive approach by combining experimental measurements and an analytical thermal model. Compared to the reported analytical approaches, a three-dimensional analytical thermal model was developed in this study. Only a single experimental setup was then necessary to study the influence of the temperature. This method was applied to a pouch cell at 50% SOC from 0 °C to 40 °C.

The cell thermal anisotropy was successfully characterized with the experimental setup. A model with adiabatic boundary conditions was first considered for calibration. The testing time had to be restricted to stay within the scope of this assumption. A model including convection boundary conditions was then used. It allowed to extend the duration of the experiment and to gather more experimental data. Both models involved similar results, although the model with convection boundary convection proved to be significantly more reliable. Indeed, it showed high fitting accuracy with the experimental data. Furthermore, the thermal parameters identified with this model followed clearer tendencies versus temperature. Especially, the heat capacity and the through-planes thermal conductivity displayed a linear behavior, which was consistent with the literature review.

This method is very flexible and is suitable for any parallelepiped-shaped battery (pouch and prismatic). With prismatic batteries, the hard cell case and the winding of the rolled sheets might involve a gap between the apparent and the actual parameters of the cell. Some works investigated this issue [40,45]. The equivalent experiment for cylindrical cells would involve wrapping a flexible heater around the cell so that the heating area is a cylinder halfway-up the cell. With this cell geometry, the analytical model needs to be developed by considering cylindrical coordinates.

Acknowledgements

This work was supported by CRITT M2A and BPI France within the scope of the OECTE project, laureate of the France Relance plan. All the experiments were performed in CRITT M2A. The authors would also like to thank the technician staff for their support.

Nomenclature

a	Size of the heating area (m)
c_p	Specific heat capacity ($J.kg^{-1}.K^{-1}$)
H	Height of the cell stack (m)
$h_{cell\text{-}air}$	Heat transfer coefficient ($W.m^{-2}.K^{-1}$)
K	Coefficients of the Fourier series (K)
L	Half-length of the cell stack (m)
$\vec{q}$	Heat flux ($W.m^{-2}$)
Q	Magnitude of heat flux ($W.m^{-2}$)
R_0	Electrical resistance of the heater (Ω)
R_1	Electrical resistance of the first resistor in the amplifier circuit (Ω)
R_2	Electrical resistance of the second resistor in the amplifier circuit (Ω)
t	Time variable (s)
W	Half-width of the cell stack (m)
U_{op}	Amplifier circuit output voltage (V)
U_Q	Heat flux sensor output voltage (V)
x	Space variable related to the cell length (m)
X	Transformed space variable x (m)
y	Space variable related to the cell width (m)
Y	Transformed space variable y (m)
z	Space variable related to the cell height (m)
Z	Transformed space variable z (m)

Greek letters

α	Eigenvalue related to variable X (m^{-1})
β	Eigenvalue related to variable Y (m^{-1})
γ	Eigenvalue related to variable Z (m^{-1})
δ	Global eigenvalue (m^{-1})
ε_{op}	Offset of the amplifier circuit (V)
θ	Temperature rise (K)
κ_{op}	Gain of the amplifier circuit (∅)
λ	Thermal conductivity ($W.m^{-1}.K^{-1}$)
Λ	Transformed thermal conductivity (∅)
ρ	Cell density ($kg.m^{-3}$)
σ_Q	Sensitivity of the heat flux sensor ($V.m^2.W^{-1}$)
τ	Time constant (s)
φ	Eigenfunction

Subscripts

∥	In-plane
⊥	Through-plane
0	Initial condition
n	Eigenfunction and eigenvalue order related to variable X
k	Eigenfunction and eigenvalue order related to variable Y
p	Eigenfunction and eigenvalue order related to variable Z
x	Relative to the cell length
y	Relative to the cell width
z	Relative to the cell height

References

[1] IEA, Global EV Outlook 2021, IEA, Paris, 2021. https://www.iea.org/reports/global-ev-outlook-2021 (accessed August 20, 2021).

[2] C.P. Grey, D.S. Hall, Prospects for lithium-ion batteries and beyond—a 2030 vision, Nat Commun. 11 (2020) 6279. https://doi.org/10.1038/s41467-020-19991-4.

[3] B. Wu, V. Yufit, M. Marinescu, G.J. Offer, R.F. Martinez-Botas, N.P. Brandon, Coupled thermal–electrochemical modelling of uneven heat generation in lithium-ion battery packs, Journal of Power Sources. 243 (2013) 544–554. https://doi.org/10.1016/j.jpowsour.2013.05.164.

[4] Y. Ye, Y. Shi, N. Cai, J. Lee, X. He, Electro-thermal modeling and experimental validation for lithium ion battery, Journal of Power Sources. 199 (2012) 227–238. https://doi.org/10.1016/j.jpowsour.2011.10.027.

[5] L. Lam, P. Bauer, E. Kelder, A practical circuit-based model for Li-ion battery cells in electric vehicle applications, in: 2011 IEEE 33rd International Telecommunications Energy Conference (INTELEC), IEEE, Amsterdam, Netherlands, 2011: pp. 1–9. https://doi.org/10.1109/INTLEC.2011.6099803.

[6] R.C. Kroeze, P.T. Krein, Electrical battery model for use in dynamic electric vehicle simulations, in: 2008 IEEE Power Electronics Specialists Conference, IEEE, Rhodes, Greece, 2008: pp. 1336–1342. https://doi.org/10.1109/PESC.2008.4592119.

[7] K. Smith, C.-Y. Wang, Power and thermal characterization of a lithium-ion battery pack for hybrid-electric vehicles, Journal of Power Sources. 160 (2006) 662–673. https://doi.org/10.1016/j.jpowsour.2006.01.038.

[8] Y.K. Tan, J.C. Mao, K.J. Tseng, Modelling of battery temperature effect on electrical characteristics of Li-ion battery in hybrid electric vehicle, in: 2011 IEEE Ninth International Conference on Power Electronics and Drive Systems, IEEE, Singapore, 2011: pp. 637–642. https://doi.org/10.1109/PEDS.2011.6147318.

[9] L. Gao, S. Liu, R.A. Dougal, Dynamic lithium-ion battery model for system simulation, IEEE Trans. Comp. Packag. Technol. 25 (2002) 495–505. https://doi.org/10.1109/TCAPT.2002.803653.

[10] T. Waldmann, M. Wilka, M. Kasper, M. Fleischhammer, M. Wohlfahrt-Mehrens, Temperature dependent ageing mechanisms in Lithium-ion batteries – A Post-Mortem study, Journal of Power Sources. 262 (2014) 129–135. https://doi.org/10.1016/j.jpowsour.2014.03.112.

[11] E. Peled, D. Golodnitsky, G. Ardel, V. Eshkenazy, The sei model—application to lithium-polymer electrolyte batteries, Electrochimica Acta. 40 (1995) 2197–2204. https://doi.org/10.1016/0013-4686(95)00163-9.

[12] J. Vetter, P. Novák, M.R. Wagner, C. Veit, K.-C. Möller, J.O. Besenhard, M. Winter, M. Wohlfahrt-Mehrens, C. Vogler, A. Hammouche, Ageing mechanisms in lithium-ion batteries, Journal of Power Sources. 147 (2005) 269–281. https://doi.org/10.1016/j.jpowsour.2005.01.006.

[13] H. Buqa, A. Würsig, J. Vetter, M.E. Spahr, F. Krumeich, P. Novák, SEI film formation on highly crystalline graphitic materials in lithium-ion batteries, Journal of Power Sources. 153 (2006) 385–390. https://doi.org/10.1016/j.jpowsour.2005.05.036.

[14] K. Edström, M. Herstedt, D.P. Abraham, A new look at the solid electrolyte interphase on graphite anodes in Li-ion batteries, Journal of Power Sources. 153 (2006) 380–384. https://doi.org/10.1016/j.jpowsour.2005.05.062.

[15] E. Peled, S. Menkin, Review—SEI: Past, Present and Future, J. Electrochem. Soc. 164 (2017) A1703. https://doi.org/10.1149/2.1441707jes.

[16] Z. Li, J. Huang, B. Yann Liaw, V. Metzler, J. Zhang, A review of lithium deposition in lithium-ion and lithium metal secondary batteries, Journal of Power Sources. 254 (2014) 168–182. https://doi.org/10.1016/j.jpowsour.2013.12.099.

[17] M. Petzl, M. Kasper, M.A. Danzer, Lithium plating in a commercial lithium-ion battery – A low-temperature aging study, Journal of Power Sources. 275 (2015) 799–807. https://doi.org/10.1016/j.jpowsour.2014.11.065.

[18] V. Agubra, J. Fergus, Lithium Ion Battery Anode Aging Mechanisms, Materials. 6 (2013) 1310–1325. https://doi.org/10.3390/ma6041310.

[19] C. Zhan, J. Lu, A. Jeremy Kropf, T. Wu, A.N. Jansen, Y.-K. Sun, X. Qiu, K. Amine, Mn(II) deposition on anodes and its effects on capacity fade in spinel lithium manganate–carbon systems, Nature Communications. 4 (2013) 2437. https://doi.org/10.1038/ncomms3437.

[20] G.-C. Chung, H.-J. Kim, S.-I. Yu, S.-H. Jun, J. Choi, M.-H. Kim, Origin of Graphite Exfoliation An Investigation of the Important Role of Solvent Cointercalation, J. Electrochem. Soc. 147 (2000) 4391. https://doi.org/10.1149/1.1394076.

[21] M. Wohlfahrt-Mehrens, C. Vogler, J. Garche, Aging mechanisms of lithium cathode materials, Journal of Power Sources. 127 (2004) 58–64. https://doi.org/10.1016/j.jpowsour.2003.09.034.

[22] S.S. Madani, E. Schaltz, S. Knudsen Kær, Heat Loss Measurement of Lithium Titanate Oxide Batteries under Fast Charging Conditions by Employing Isothermal Calorimeter, Batteries. 4 (2018) 59. https://doi.org/10.3390/batteries4040059.

[23] J. Zhang, L. Zhang, F. Sun, Z. Wang, An Overview on Thermal Safety Issues of Lithium-ion Batteries for Electric Vehicle Application, IEEE Access. 6 (2018) 23848–23863. https://doi.org/10.1109/ACCESS.2018.2824838.

[24] C.A. Karthik, P. Kalita, X. Cui, X. Peng, Thermal management for prevention of failures of lithium ion battery packs in electric vehicles: A review and critical future aspects, Energy Storage. 2 (2020) e137. https://doi.org/10.1002/est2.137.

[25] J. Zhao, Z. Rao, Y. Huo, X. Liu, Y. Li, Thermal management of cylindrical power battery module for extending the life of new energy electric vehicles, Applied Thermal Engineering. 85 (2015) 33–43. https://doi.org/10.1016/j.applthermaleng.2015.04.012.

[26] R. Kizilel, R. Sabbah, J.R. Selman, S. Al-Hallaj, An alternative cooling system to enhance the safety of Li-ion battery packs, Journal of Power Sources. 194 (2009) 1105–1112. https://doi.org/10.1016/j.jpowsour.2009.06.074.

[27] H. Maleki, S.A. Hallaj, J.R. Selman, R.B. Dinwiddie, H. Wang, Thermal Properties of Lithium-Ion Battery and Components, J. Electrochem. Soc. 146 (1999) 947. https://doi.org/10.1149/1.1391704.

[28] L. Song, Y. Chen, J.W. Evans, Measurements of the Thermal Conductivity of Poly(ethylene oxide)-Lithium Salt Electrolytes, J. Electrochem. Soc. 144 (1997) 3797. https://doi.org/10.1149/1.1838094.

[29] F. Richter, S. Kjelstrup, P.J.S. Vie, O.S. Burheim, Thermal conductivity and internal temperature profiles of Li-ion secondary batteries, Journal of Power Sources. 359 (2017) 592–600. https://doi.org/10.1016/j.jpowsour.2017.05.045.

[30] Y. Saito, K. Kanari, K. Takano, T. Masuda, A calorimetric study on a cylindrical type lithium secondary battery by using a twin-type heat conduction calorimeter, Thermochimica Acta. 296 (1997) 75–85. https://doi.org/10.1016/S0040-6031(97)00083-X.

[31] A.A. Pesaran, M. Keyser, Thermal characteristics of selected EV and HEV batteries, in: Sixteenth Annual Battery Conference on Applications and Advances. Proceedings of the Conference (Cat. No.01TH8533), Long Beach, CA, USA, 2001: pp. 219–225. https://doi.org/10.1109/BCAA.2001.905129.

[32] G. Yu, X. Zhang, C. Wang, W. Zhang, C. Yang, Experimental Study on Specific Heat Capacity of Lithium Thionyl Chloride Batteries by a Precise Measurement Method, J. Electrochem. Soc. 160 (2013) A985. https://doi.org/10.1149/2.148306jes.

[33] N.S. Spinner, R. Mazurick, A. Brandon, S.L. Rose-Pehrsson, S.G. Tuttle, Analytical, Numerical and Experimental Determination of Thermophysical Properties of Commercial 18650 LiCoO2 Lithium-Ion Battery, J. Electrochem. Soc. 162 (2015) A2789. https://doi.org/10.1149/2.0871514jes.

[34] S.J. Bazinski, X. Wang, Experimental study on the influence of temperature and state-of-charge on the thermophysical properties of an LFP pouch cell, Journal of Power Sources. 293 (2015) 283–291. https://doi.org/10.1016/j.jpowsour.2015.05.084.

[35] K.A. Murashko, A.V. Mityakov, J. Pyrhönen, V.Y. Mityakov, S.S. Sapozhnikov, Thermal parameters determination of battery cells by local heat flux measurements, Journal of Power Sources. 271 (2014) 48–54. https://doi.org/10.1016/j.jpowsour.2014.07.117.

[36] L. Sheng, L. Su, H. Zhang, Experimental determination on thermal parameters of prismatic lithium ion battery cells, International Journal of Heat and Mass Transfer. 139 (2019) 231–239. https://doi.org/10.1016/j.ijheatmasstransfer.2019.04.143.

[37] S.J. Drake, D.A. Wetz, J.K. Ostanek, S.P. Miller, J.M. Heinzel, A. Jain, Measurement of anisotropic thermophysical properties of cylindrical Li-ion cells, Journal of Power Sources. 252 (2014) 298–304. https://doi.org/10.1016/j.jpowsour.2013.11.107.

[38] K.A. Murashko, J. Pyrhönen, J. Jokiniemi, Determination of the through-plane thermal conductivity and specific heat capacity of a Li-ion cylindrical cell, International Journal of Heat and Mass Transfer. 162 (2020) 120330. https://doi.org/10.1016/j.ijheatmasstransfer.2020.120330.

[39] M. Akbarzadeh, T. Kalogiannis, J. Jaguemont, J. He, L. Jin, M. Berecibar, J. Van Mierlo, Thermal modeling of a high-energy prismatic lithium-ion battery cell and module based on a new thermal characterization methodology, Journal of Energy Storage. 32 (2020) 101707. https://doi.org/10.1016/j.est.2020.101707.

[40] M. Steinhardt, E.I. Gillich, M. Stiegler, A. Jossen, Thermal conductivity inside prismatic lithium-ion cells with dependencies on temperature and external compression pressure, Journal of Energy Storage. 32 (2020) 101680. https://doi.org/10.1016/j.est.2020.101680.

[41] J. Zhang, B. Wu, Z. Li, J. Huang, Simultaneous estimation of thermal parameters for large-format laminated lithium-ion batteries, Journal of Power Sources. 259 (2014) 106–116. https://doi.org/10.1016/j.jpowsour.2014.02.079.

[42] M. Al-Zareer, A. Michalak, C. Da Silva, C.H. Amon, Predicting specific heat capacity and directional thermal conductivities of cylindrical lithium-ion batteries: A combined experimental and simulation framework, Applied Thermal Engineering. 182 (2021) 116075. https://doi.org/10.1016/j.applthermaleng.2020.116075.

[43] N. Damay, C. Forgez, M.-P. Bichat, G. Friedrich, Thermal modeling of large prismatic LiFePO4/graphite battery. Coupled thermal and heat generation models for characterization and simulation, Journal of Power Sources. 283 (2015) 37–45. https://doi.org/10.1016/j.jpowsour.2015.02.091.

[44] T.S. Bryden, B. Dimitrov, G. Hilton, C. Ponce de León, P. Bugryniec, S. Brown, D. Cumming, A. Cruden, Methodology to determine the heat capacity of lithium-ion cells, Journal of Power Sources. 395 (2018) 369–378. https://doi.org/10.1016/j.jpowsour.2018.05.084.

[45] D. Werner, A. Loges, D.J. Becker, T. Wetzel, Thermal conductivity of Li-ion batteries and their electrode configurations – A novel combination of modelling and experimental approach, Journal of Power Sources. 364 (2017) 72–83. https://doi.org/10.1016/j.jpowsour.2017.07.105.